SIAM J. Imaging Sciences
Vol. 9, No. 2, pp. 520–536

Exact Inversion of the Cone Transform Arising in an Application of a Compton Camera Consisting of Line Detectors*

Chang-Yeol Jung† and Sunghwan Moon‡

Abstract. A Compton camera has been suggested for use in single photon emission computed tomography because a conventional gamma camera has low efficiency. Here we consider a cone transform brought about by a Compton camera with line detectors. A cone transform takes a given function on the 3-dimensional space and assigns to it the surface integral of the function over cones determined by the 1-dimensional vertex space, the 1-dimensional central axis, and the 1-dimensional opening angle. We generalize this cone transform to n-dimensional space and provide an inversion formula. Also, numerical simulations are presented to demonstrate our suggested algorithm in three dimensions.

Key words. Compton camera, SPECT, tomography, cone transform, inversion, gamma camera

AMS subject classifications. 44A12, 65R10, 92C55

DOI. 10.1137/15M1033617

1. Introduction.

A Radon-type transform that assigns to a given function its surface integral over various sets of cones has been studied, since it is known that this kind of a transform relates to a *Compton camera*. A Compton camera, also called an *electronically collimated γ-camera*, was introduced for use in *single photon emission computed tomography* (SPECT) because of the low efficiency of a conventional γ-camera [26, 32]. A Compton camera has very high sensitivity and flexibility of geometrical design, so it has attracted a lot of interest and applications in many areas including monitoring nuclear power plants and astronomy [1, 3].

A standard Compton camera consists of two planar detectors: a scatter detector and an absorption detector, positioned one behind the other. A photon emitted from a radioactive source toward the camera undergoes Compton scattering in the scatter detector, and is absorbed in the absorption detector positioned behind (see Figure 1). In each detector, the position of the hit and the energy of the photon are measured. The scattering angle or the

*Received by the editors August 3, 2015; accepted for publication (in revised form) February 3, 2016; published electronically April 7, 2016.

http://www.siam.org/journals/siims/9-2/M103361.html

†Department of Mathematical Sciences, Ulsan National Institute of Science and Technology, Ulsan 44919, Republic of Korea (cjung@unist.ac.kr). The research of this author was supported under the framework of international cooperation program managed by the National Research Foundation of Korea (2015K2A1A2070543) and supported by the National Research Foundation of Korea funded by the Ministry of Education (2015R1D1A1A01059837).

‡Department of Mathematical Sciences, Ulsan National Institute of Science and Technology, Ulsan 44919, Republic of Korea (shmoon@unist.ac.kr). The research of this author was supported by the National Research Foundation of Korea grant funded by the Korea government (MSIP) (2015R1C1A1A01051674) and supported by the TJ Park Science Fellowship of POSCO TJ Park Foundation.

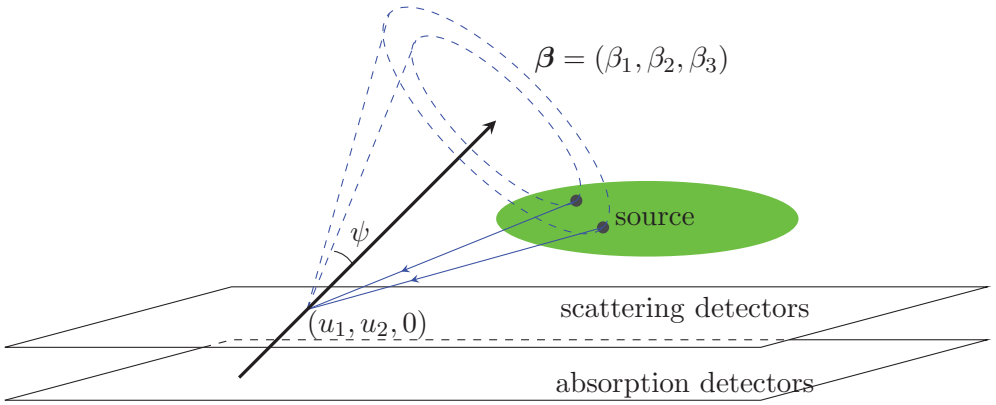

Figure 1. *Schematic representation of a standard Compton camera.*

opening angle ψ can be computed from the measured energies and electron mass as follows:

$$\cos\psi = 1 - \frac{mc^2\Delta E}{(E-\Delta E)E}, \tag{1.1}$$

where m is the mass of the electron, c is the speed of light, E is the initial γ-ray energy, and ΔE is the energy transferred to the electron in the scattering process [1, 7, 19].

When $f(x,y,z)$ is the distribution of the radioactive source, the intensity of the photon measured by the detector is given by

$$I = \int_L f(x,y,z) \exp\left\{ - \int_{L(x,y,z)} \mu(x',y',z') dx'dy'dz' \right\} dxdydz,$$

where L is the straight line the photon follows and $L(x,y,z)$ is the section of L between (x,y,z) and the detector. Here μ is the attenuation coefficient of the medium the photon is passing through [22, Chapter 1]. SPECT, a nuclear imaging test, uses a radioactive substance to show how blood flows to tissues and organs. Thus, in SPECT, we are interested in f, not in μ. If the medium is very thin or its attenuation coefficient is very small in order for μ to be negligible, the intensity I is essentially the line integral of f. In this article, we assume μ is negligible.

In fact, one does not know the exact incoming direction of the detected photon and thus, a cone is introduced as possible incoming directions of the photon (see Figure 1). Therefore, we get the conical projection which is the surface integral of the distribution of the radiation source over cones with a central axis $\boldsymbol{\beta}$ (obtained by a difference vector between the scattering and absorbing positions), a vertex $(u_1, u_2, 0)$ at the scattering position, and an opening angle ψ obtained by (1.1). Thus, the surface integral of a source distribution over a family of cones is referred to as a *cone transform*.

Here, we consider a Compton camera consisting of two linear detectors. If the linear detectors are assumed to be set along the x-axis, then the vertex has zero in the second coordinate, i.e., $u_2 = 0$ and the central axis $\boldsymbol{\beta} = (\beta_1, \beta_2, \beta_3) \in S^2$ has zero in the second coordinate, i.e., $\beta_2 = 0$ (see Figure 2).

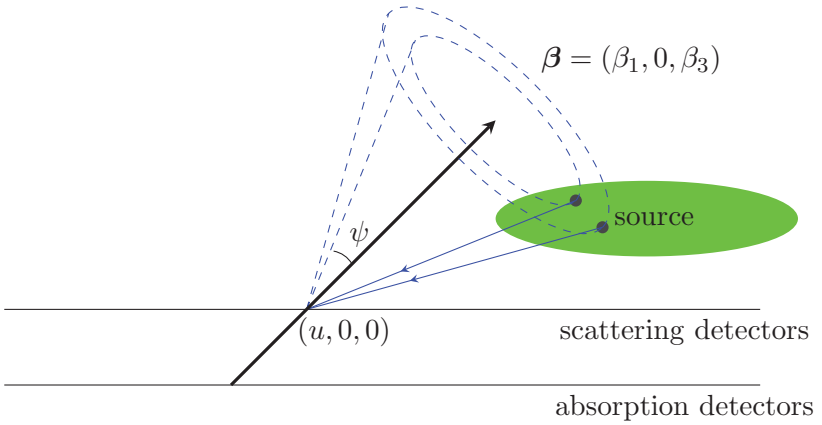

Figure 2. *Schematic representation of a Compton camera with line detectors.*

Generally, it is easier to set linear detectors than to set planar detectors (the standard Compton camera) because the former requires one less dimension in physical space. In other words, the linear detectors require a much smaller number of detectors in space to detect, e.g., a widely spread source. Thus, linear detectors are very economical and preferred to planar detectors. Indeed, the reduction of dimensions significantly reduces costs both in physical space for the detectors and in data space and storage for the measured data obtained from the Compton camera. The planar detectors require 5 dimensions ($\boldsymbol{\beta} \in S^2,\ (u_1, u_2, 0),\ \psi$), whereas the linear detectors require only 3 dimensions ($(\beta_1, 0, \beta_3) \in S^1,\ (u, 0, 0),\ \psi$).

Regarding the data space, due to the high volume of data obtained from the planar detectors (5 dimensions), one tries to use only partial data for efficiency in implementations (see, e.g., [2, 5, 6, 13, 21, 25, 28]), but it requires considerable costs to store unnecessary data and this also causes additional costs to retrieve the target data. The Compton camera usually carries considerable noise in applications and utilizing full 5 dimensional data is advised to obtain accurate numerical results (see, e.g., [1]) although significant computational time and resources should be required. On the other hand, the linear detectors save the data space and storage as well by 2 dimensions and this makes it very efficient to retrieve and manipulate the data.

However, we note that there can be some sensitivity issues in numerically implementing the inversion formula. Basically, the data acquisition in a Compton camera with linear detectors is the same as in the standard one. The only difference between these two types of Compton camera settings is that the available data are restricted for the linear detectors because the vertex of their cones moves only on a line. While the planar detectors are aligned on one side of a plane, the line detectors along a line in the plane can be aligned in infinitely many ways. Depending on the configurations between the line detectors and the radioactive source, the available data will vary and hence the numerical inversion results will show some varying artifacts and numerical errors in some parts.

Several inversion formulas for various types of cone transforms were derived in [2, 5, 6, 11, 12, 13, 16, 19, 21, 24, 25, 28, 31, 34]. The cone transform with planar vertex positions and a fixed central axis was studied in [5, 6, 16, 21, 24, 25, 34]. Haltme ier derived an exact backprojection-type inversion formula for the n-dimensional cone transform which integrates

a given n-dimensional function over all conical surfaces having vertices on a hyperplane and a central axis orthogonal to this hyperplane in [13]. Some works [11, 12] studied the cone transform with a fixed opening angle and a fixed central axis. They demonstrated that an explicit 2-dimensional inversion formula they derived is feasible in numerical applications.

The rest of this paper is organized as follows. The definition is formulated precisely in section 2. Section 3 is devoted to the n-dimensional cone transform and its inversion formula. Finally, we provide numerical simulations to demonstrate the suggested 3-dimensional algorithm in section 4.

2. The 3-dimensional cone transform. In this section we formulate the cone transform with line detectors in space dimension 3. Let $f(x, y, z)$ be the distribution of the radioactivity sources. It is often assumed that $f(x, y, z)$ is supported on one side of the Compton camera in real applications. With planar detectors, it is usually assumed that the support of f is contained in the upper half-space $\{(x, y, z) \in \mathbb{R}^3 : z > 0\}$. However, with linear detectors, since a line does not separate $\mathbb{R}^3$, the support of f could be anywhere away from the line. If f is odd with respect to y, the cone transform $\mathbf{C}f$ as defined in (2.1) produces nothing, i.e., $\mathbf{C}f = 0$, which is explained below in this section. This naturally lets us assume that f is supported in $\{(x, y, z) \in \mathbb{R}^3 : y > 0\}$ or $\{(x_1, x_2, \ldots, x_n) \in \mathbb{R}^n : x_2 > 0\}$ (see Theorem 5 below). Let $\boldsymbol{\beta} = (\beta_1, \beta_2, \beta_3) \in S^2$ be a central axis and $\psi \in [0, \pi]$ be an opening angle. It is assumed that scatter and absorption detectors are set along the x-axis and the line parallel to the x-axis, respectively. Thus we let $(u, 0, 0)$ be the position of the scatter detectors and β_2 be zero, i.e., $\boldsymbol{\beta} = (\beta_1, 0, \beta_3) \in S^1$. Here and after in the analysis we often need only (β_1, β_3) as the unit vector in S^1. To distinguish $\boldsymbol{\beta} \in S^2$ and $(\beta_1, \beta_3) \in S^1$, for convenience we introduce a new notation $\bar{\boldsymbol{\beta}} = (\beta_1, \beta_3) \in S^1$.

As also explained in the introduction, our cones are parameterized by u determining a vertex $(u, 0, 0)$, a parameter $\bar{\boldsymbol{\beta}}$ determining a central axis $\boldsymbol{\beta}$, and an opening angle ψ (see Figure 2) as possible directions, although the exact incoming direction of the detected photon is not available. Thus the data measured by a Compton camera can be represented as the integral of the source distribution over cones described above:

$$\mathbf{C}f(u, \bar{\boldsymbol{\beta}}, \psi) = K(\psi) \sin\psi \int_{S^2} \int_0^\infty f((u, 0, 0) + r\boldsymbol{\alpha}) r \delta(\boldsymbol{\alpha} \cdot \boldsymbol{\beta} - \cos\psi) dr dS(\boldsymbol{\alpha}), \tag{2.1}$$

where δ is the Dirac delta function and $dS(\boldsymbol{\alpha})$ is the standard area measure on the unit sphere S^2 (see Figure 3), i.e.,

$$dS(\boldsymbol{\alpha}) = \delta\Big(1 - \sqrt{\alpha_1^2 + \alpha_2^2 + \alpha_3^2}\Big) d\alpha_1 d\alpha_2 d\alpha_3, \quad \boldsymbol{\alpha} = (\alpha_1, \alpha_2, \alpha_3) \in \mathbf{R}^3.$$

Here $K(\psi)$ is the (known) Klein–Nishina coefficient.

To see the appearance of the factor $\sin\psi$, we consider the spherical coordinates on S^2 (see Figure 3) which define θ to be the polar angle $(0 \le \theta \le \pi)$ (also known as the zenith angle) from the central axis $\boldsymbol{\beta}$ and ϕ to be the azimuthal angle $(0 \le \phi < 2\pi)$ in the plane normal to the central axis. Since $\boldsymbol{\alpha} \cdot \boldsymbol{\beta} = \cos\theta$ and $dS(\boldsymbol{\alpha}) = \sin\theta d\theta d\phi$, the right-hand side of (2.1)

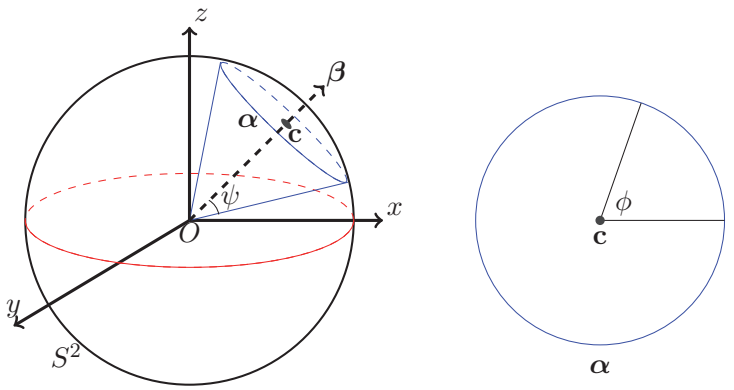

Figure 3. *A circle $\boldsymbol{\alpha}$ in the unit sphere.*

except $K(\psi)$ can then be written as

$$
\begin{aligned}
&\sin\psi \int_0^\infty \int_0^{2\pi} \int_0^\pi f((u,0,0)+r\boldsymbol{\alpha}(\phi))r\delta(\cos\theta-\cos\psi)\sin\theta d\theta d\phi dr \\
&= \sin\psi \int_0^\infty \int_0^{2\pi} \int_{-1}^1 f((u,0,0)+r\boldsymbol{\alpha}(\phi))r\delta(t-\cos\psi)dtd\phi dr \\
&= \int_0^{2\pi} \int_0^\infty f((u,0,0)+r\boldsymbol{\alpha}(\phi))r\sin\psi drd\phi, \quad \boldsymbol{\alpha}\cdot\boldsymbol{\beta}=\cos\psi, \boldsymbol{\alpha}\in S^2.
\end{aligned} \tag{2.2}
$$

where in the second line, we used the change of variables $t=\cos\theta$ and $dt=-\sin\theta d\theta$. Here $\boldsymbol{\alpha}$, the function from $[0,2\pi)$ to S^2, is the circle on the unit sphere with distance $\sqrt{1-s^2}$ from the central axis $\boldsymbol{\beta}=(\beta_1,0,\beta_3)\in S^2$ (see Figure 3). We notice that the area measure on the cone characterized by $(u,\bar{\boldsymbol{\beta}},\psi)$ is $r\sin\psi drd\phi$ as in the last integral. As the central axis $\boldsymbol{\beta}$ is in the x-z plane, if f is odd with respect to y and ϕ is measured counterclockwise as in Figure 3, we note that $(\alpha_1,\alpha_2,\alpha_3)(-\phi)=(\alpha_1,-\alpha_2,\alpha_3)(\phi)$ and hence $f((u,0,0)+r\boldsymbol{\alpha}(-\phi))=-f((u,0,0)+r\boldsymbol{\alpha}(\phi))$. The last integral is then zero which gives $\mathbf{C}f=0$. Since the known function $K(\psi)\sin\psi$ can be easily handled, we will not take it into account further in the analysis. Dropping it and raising the power k of r we thus consider a more general form of a cone transform $\mathbf{C}f$, which is

$$
\mathbf{C}^k f(u,\bar{\boldsymbol{\beta}},\psi)=\int_{S^2}\int_0^\infty f((u,0,0)+r\boldsymbol{\alpha})r^k\delta(\boldsymbol{\alpha}\cdot\boldsymbol{\beta}-\cos\psi)drdS(\boldsymbol{\alpha}) \tag{2.3}
$$

for $k\geq 0$ (physically, it is almost impossible for k to be negative). Also, we assume that the density of the photons decreases at the 1:1 rate of distance from the source to detectors in the case of C^1f. When the density decreases as a different power of distance, we need a different power of r (see, e.g., [16]).

For simplicity, set $s=\cos\psi\in[-1,1]$, and define the cone transform C^k of a function $f\in C(\mathbb{R}^3)$ with compact support by

$$
C^k f(u,\bar{\boldsymbol{\beta}},s):=\begin{cases}\mathbf{C}^k f(u,\bar{\boldsymbol{\beta}},\arccos s) \\ \quad =\displaystyle\int_{S^2}\int_0^\infty f((u,0,0)+r\boldsymbol{\alpha})r^k\delta(\boldsymbol{\alpha}\cdot\boldsymbol{\beta}-s)drdS(\boldsymbol{\alpha}) & \text{if } s\in[-1,1], \\ 0 & \text{otherwise.}\end{cases} \tag{2.4}
$$

We write $\mathbf{C}^1f=\mathbf{C}f$ and $C^1f=Cf$.

In the next section, we introduce an n-dimensional cone transform C^k. After defining a new Radon-type transform, the weighted ray transform, we show how $C^k f$ can be reduced to the weighted ray transform. By deriving the inversion formula for the weighted ray transform, we obtain an inversion formula for the cone transform $C^k f$. Finally, we perform numerical simulations to demonstrate the efficiency of the suggested algorithm in 3 dimensions.

3. Exact inversion formula.

As mentioned before, we generalize the cone transform $C^k f$ to an n-dimensional case and define the weighted ray transform. We first find the inversion formula for the weighted ray transform and show how to reduce $C^k f$ to the weighted ray transform. Combining these two steps, we obtain the inversion formula for $C^k f$.

Definition 1. *Let $n \geq 3$.*

- *Suppose that f is a continuous function and is compactly supported in*

$$\{\mathbf{x} = (x_1, x_2, \ldots, x_n) \in \mathbb{R}^n : x_2 > 0\}.$$

For $k \geq 0$, the cone transform C^k maps f into

$$C^k f(u, \bar{\boldsymbol{\beta}}, s) = \int_{S^{n-1}} \int_0^\infty f((u, 0, \ldots, 0) + r\boldsymbol{\alpha}) r^k \delta(\boldsymbol{\alpha} \cdot \boldsymbol{\beta} - s) dr dS(\boldsymbol{\alpha})$$

for $(u, \bar{\boldsymbol{\beta}}, s) \in \mathbb{R} \times S^{n-2} \times [-1, 1]$. Here $\bar{\boldsymbol{\beta}} = (\beta_1, \beta_3, \ldots, \beta_n) \in S^{n-2}$, $\boldsymbol{\beta} = (\beta_1, 0, \beta_3, \ldots, \beta_n) \in S^{n-1}$, $dS(\boldsymbol{\alpha})$ is the standard area measure on the unit sphere in $\mathbb{R}^n$, and δ is the Dirac delta function.

- *Suppose that f is a continuous function and is compactly supported in $\mathbb{R}^n$. For $k \geq 0$, the n-dimensional weighted ray transform P_k maps f into*

$$P_k f(u, \mathbf{w}) = \int_0^\infty f((u, 0, \ldots, 0) + r\mathbf{w}) r^k dr$$

for $(u, \mathbf{w}) = (u, w_1, w_2, \ldots, w_n) \in \mathbb{R} \times [\mathbb{R}^n \setminus \{\mathbf{0}\}]$.

We notice that $P_0 f$ becomes the cone beam transform, also known as the divergent beam transform, which is one of the classic problems in computed tomography. There are many works discussing this [9, 10, 27, 29, 30, 33].

Before finding the inversion formula for the weighted ray transform $P_k f$, we define a linear operator $I^\kappa_{x_1}, \kappa < 1$, by

$$\mathcal{F}_{x_1 \to \xi}[I^\kappa_{x_1} f](\xi, \boldsymbol{x}) = |\xi|^{-\kappa} \mathcal{F}_{x_1 \to \xi} f(\xi, \boldsymbol{x}),$$

where $\mathbf{x} = (x_1, \boldsymbol{x}) \in \mathbb{R} \times \mathbb{R}^{n-1}$ and $\mathcal{F}_{x_1 \to \xi} f$ is the 1-dimensional Fourier transform of f with respect to x_1. (This operator is known as the (partial) Riesz potential.)

Lemma 2. *Let $\kappa < 1$. If $f(\mathbf{x}) \in C^\infty(\mathbb{R}^n)$, $n \geq 3$, has compact support in $\mathbb{R}^n$, then we have for $x_2 > 0$*

$$I^\kappa_{x_1} f(\mathbf{x}) = 2^{-1} \pi^{-1} \int_{\mathbb{R}} I^{\kappa-1}_u P_k f(x_1 - w_1, w_1, \boldsymbol{x}) dw_1. \tag{3.1}$$

This proof follows the idea suggested in [20].

Proof. Taking the 1-dimensional Fourier transform of $P_k f(u, \mathbf{w})$ with respect to u yields

$$\int_{\mathbb{R}} P_k f(u, \mathbf{w}) e^{-i\xi u} du = \int_0^\infty \mathcal{F}_{x_1 \to \xi} f(\xi, rw_2, rw_3, \dots, rw_n) e^{irw_1 \xi} r^k dr.$$

To get $\mathcal{F}_{x_1 \to \xi} f$, multiply $e^{-iw_1 \xi}$ and integrate with respect to w_1. Then we have

$$\int_{\mathbb{R}} \int_{\mathbb{R}} P_k f(u, \mathbf{w}) e^{-i(w_1+u)\xi} du dw_1 = \int_{\mathbb{R}} \int_0^\infty \mathcal{F}_{x_1 \to \xi} f(\xi, rw_2, \dots, rw_n) e^{irw_1 \xi} r^k e^{-iw_1 \xi} dr dw_1.$$

Changing the variables $w_1 \xi \to w_1$ gives

$$\begin{aligned}
\int_{\mathbb{R}} \int_{\mathbb{R}} P_k f(u, \mathbf{w}) e^{-i(w_1+u)\xi} du dw_1 &= \int_{\mathbb{R}} \int_0^\infty \mathcal{F}_{x_1 \to \xi} f(\xi, rw_2, \dots, rw_n) r^k e^{i(r-1)w_1} dr \frac{dw_1}{|\xi|} \\
&= \int_0^\infty \mathcal{F}_{x_1 \to \xi} f(\xi, rw_2, \dots, rw_n) r^k \int_{\mathbb{R}} e^{i(r-1)w_1} dw_1 \frac{dr}{|\xi|} \\
&= 2\pi \int_0^\infty \mathcal{F}_{x_1 \to \xi} f(\xi, rw_2, \dots, rw_n) r^k \delta(r-1) \frac{dr}{|\xi|}.
\end{aligned}$$

Therefore, we have

$$\int_{\mathbb{R}} \int_{\mathbb{R}} |\xi|^{-\kappa+1} P_k f(u, \mathbf{w}) e^{-i(w_1+u)\xi} du dw_1 = 2\pi \mathcal{F}_{x_1 \to \xi} f(\xi, w_2, \dots, w_n) |\xi|^{-\kappa}.$$

■

Remark 3. *Let* $\mathbf{x} = (x_1, \boldsymbol{x}) \in \mathbb{R} \times \mathbb{R}^{n-1}$. *When* $\kappa = 0$, (3.1) *becomes*

$$f(\mathbf{x}) = 2^{-1} \pi^{-1} \int_{\mathbb{R}} H_u \partial_u P_k f(x_1 - w_1, w_1, \boldsymbol{x}) dw_1, \tag{3.2}$$

where $H_u h$ *is the Hilbert transform of* h *with respect to* u, *i.e.,*

$$H_u h(t) = \frac{1}{\pi} P.V. \int_{\mathbb{R}} \frac{h(u)}{t-u} du, \text{ and } P.V. \text{ is the Cauchy principal value.} \tag{3.3}$$

Here the integral in (3.2) *is a backprojection in the sense that all the rays, characterized by the parameters* $(x_1 - w_1, w_1, \boldsymbol{x})$, *travel through the reconstruction point* $\mathbf{x}$.

Proposition 4. *The operator* $C^{k,*} g$ *for* $g \in C^\infty(\mathbb{R} \times S^{n-2} \times [-1, 1])$, *defined by*

$$C^{k,*} g(\mathbf{x}) = \int_{S^{n-2}} \int_{\mathbb{R}} g\left(x_1 - u, \bar{\boldsymbol{\beta}}, \frac{\bar{\boldsymbol{\beta}} \cdot (u, x_3, \dots, x_n)}{|(u, \boldsymbol{x})|}\right) |(u, \boldsymbol{x})|^{k-n+1} du dS(\bar{\boldsymbol{\beta}})$$

for all $\mathbf{x} = (x_1, \boldsymbol{x}) \in \mathbb{R} \times \mathbb{R}^{n-1}$ *such that the integral exists, is a dual operator to* C^k, *i.e.,*

$$(C^k f,\ g)_{L^2(\mathbb{R} \times S^{n-2} \times [-1,1])} = (f,\ C^{k,*} g)_{L^2(\mathbb{R}^n)}. \tag{3.4}$$

Here $(\cdot, \cdot)_{L^2(\Omega)}$ is the standard inner product in $L^2(\Omega)$.

Proof. We start with the left-hand side of (3.4):

$$\begin{aligned}
&\int_{-1}^{1}\int_{S^{n-2}}\int_{\mathbb{R}} g(u,\bar{\boldsymbol{\beta}},s)C^k f(u,\bar{\boldsymbol{\beta}},s)dudS(\bar{\boldsymbol{\beta}})ds\\
&\quad=\int_{-1}^{1}\int_{S^{n-2}}\int_{\mathbb{R}}\int_{S^{n-1}}\int_{0}^{\infty} g(u,\bar{\boldsymbol{\beta}},s)f((u,0,\dots,0)+r\boldsymbol{\alpha})r^k\delta(\boldsymbol{\alpha}\cdot\boldsymbol{\beta}-s)drdS(\boldsymbol{\alpha})dudS(\bar{\boldsymbol{\beta}})ds\\
&\quad=\int_{-1}^{1}\int_{S^{n-2}}\int_{\mathbb{R}}\int_{\mathbb{R}^n} g(u,\bar{\boldsymbol{\beta}},s)f((u,0,\dots,0)+\mathbf{y})|\mathbf{y}|^{k-n+2}\delta(\mathbf{y}\cdot\boldsymbol{\beta}-s|\mathbf{y}|)d\mathbf{y}dudS(\bar{\boldsymbol{\beta}})ds,
\end{aligned}$$

where in the last line, we changed the polar coordinate $(r,\boldsymbol{\alpha})\in[0,\infty)\times S^{n-1}$ to the Cartesian coordinate $\mathbf{y}\in\mathbb{R}^n$. Changing the variables $(u,0,\dots,0)+\mathbf{y}\to\mathbf{x}$ gives us

$$\begin{aligned}
&\int_{-1}^{1}\int_{S^{n-2}}\int_{\mathbb{R}} g(u,\bar{\boldsymbol{\beta}},s)C^k f(u,\bar{\boldsymbol{\beta}},s)dudS(\bar{\boldsymbol{\beta}})ds\\
&\quad=\int_{-1}^{1}\int_{S^{n-2}}\int_{\mathbb{R}}\int_{\mathbb{R}^n} g(u,\bar{\boldsymbol{\beta}},s)f(\mathbf{x})|(x_1-u,\boldsymbol{x})|^{k-n+2}\\
&\qquad\times\delta((x_1-u,\boldsymbol{x})\cdot\boldsymbol{\beta}-s|(x_1-u,\boldsymbol{x})|)d\mathbf{x}dudS(\bar{\boldsymbol{\beta}})ds\\
&\quad=\int_{\mathbb{R}^n}\int_{-1}^{1}\int_{S^{n-2}}\int_{\mathbb{R}} g(u,\bar{\boldsymbol{\beta}},s)f(\mathbf{x})|(x_1-u,\boldsymbol{x})|^{k-n+2}\\
&\qquad\times\delta((x_1-u,\boldsymbol{x})\cdot\boldsymbol{\beta}-s|(x_1-u,\boldsymbol{x})|)dudS(\bar{\boldsymbol{\beta}})dsd\mathbf{x}\\
&\quad=\int_{\mathbb{R}^n} f(\mathbf{x})\left(\int_{-1}^{1}\int_{S^{n-2}}\int_{\mathbb{R}} g(x_1-u,\bar{\boldsymbol{\beta}},s)|(u,\boldsymbol{x})|^{k-n+2}\delta((u,\boldsymbol{x})\cdot\boldsymbol{\beta}-s|(u,\boldsymbol{x})|)dudS(\bar{\boldsymbol{\beta}})ds\right)d\mathbf{x},
\end{aligned}$$

where in the last line, we changed the variables $u\to x_1-u$. Computing the Dirac delta function in the inner parentheses completes our proof. ∎

Now, we provide the inversion formula for the cone transform $C^k f$.

Theorem 5. *Let $\kappa<1$ and $f\in C^\infty(\mathbb{R}^n)$, $n\geq 3$, have compact support in*

$$\{\mathbf{x}=(x_1,\boldsymbol{x})\in\mathbb{R}\times\mathbb{R}^{n-1}:x_2>0\}.$$

Then for $x_2\geq 0$, we have

(3.5)

$$f(\mathbf{x})=\frac{x_2}{2(2\pi)^{n-1}}\begin{cases}(-1)^{\frac{n-3}{2}}I_{x_1}^{-\kappa}C^{k,*}[I_u^{\kappa-1}H_s\partial_s^{n-2}C^k f\left(u,\bar{\boldsymbol{\beta}},s\right)|(x_1-u,\boldsymbol{x})|^{-2k+n-3}](\mathbf{x})\\ \qquad \text{if } n \text{ is odd},\\ (-1)^{\frac{n-2}{2}}I_{x_1}^{-\kappa}C^{k,*}[I_u^{\kappa-1}\partial_s^{n-2}C^k f\left(u,\bar{\boldsymbol{\beta}},s\right)|(x_1-u,\boldsymbol{x})|^{-2k+n-3}](\mathbf{x})\\ \qquad \text{if } n \text{ is even}.\end{cases}$$

Proof. Note that $P_k f(u,\boldsymbol{\alpha})$ is equal to zero for $\alpha_2\leq 0$ since f is compactly supported in $\{\mathbf{x}\in\mathbb{R}^n:x_2>0\}$. Hence we have for $|\boldsymbol{y}|\leq 1$, $\boldsymbol{y}=(y_1,\dots,y_{n-1})\in\mathbb{R}^{n-1}$,

$$P_k f\left(u,y_1,-\sqrt{1-|\boldsymbol{y}|^2},y_2,\dots,y_{n-1}\right)=0. \tag{3.6}$$

By the definition of $C^k f$, we can write

$$\begin{aligned} C^k f(u,\bar{\boldsymbol{\beta}},s) &= \int_{S^{n-1}} \int_0^\infty f((u,0,\dots,0)+r\boldsymbol{\alpha}) r^k \delta(\boldsymbol{\alpha}\cdot\boldsymbol{\beta}-s) dr dS(\boldsymbol{\alpha}) \\ &= \int_{S^{n-1}} P_k f(u,\boldsymbol{\alpha}) \delta(\boldsymbol{\alpha}\cdot\boldsymbol{\beta}-s) dS(\boldsymbol{\alpha}) \\ &= \int_{\substack{\boldsymbol{y}\in\mathbb{R}^{n-1} \\ |\boldsymbol{y}|\le 1}} P_k f\left(u, y_1, \sqrt{1-|\boldsymbol{y}|^2}, y_2, \dots, y_{n-1}\right) \delta(\boldsymbol{y}\cdot\bar{\boldsymbol{\beta}}-s) \frac{d\boldsymbol{y}}{\sqrt{1-|\boldsymbol{y}|^2}} \\ &= R[\Phi(u,\cdot)](\bar{\boldsymbol{\beta}},s), \end{aligned}$$

where

$$\Phi(u,\boldsymbol{y}) = \begin{cases} P_k f\left(u, y_1, \sqrt{1-|\boldsymbol{y}|^2}, y_2, \dots, y_{n-1}\right) / \sqrt{1-|\boldsymbol{y}|^2} & \text{if} \quad |\boldsymbol{y}|<1, \\ 0 & \text{otherwise} \end{cases}$$

is supported in $\{\boldsymbol{y}\in\mathbb{R}^{n-1} : |\boldsymbol{y}|\le 1\}$ and $R\Phi$ is the $(n-1)$-dimensional regular Radon transform of Φ, i.e.,

$$R[\Phi(u,\cdot)](\bar{\boldsymbol{\beta}},s) = \int_{\mathbb{R}^{n-1}} \Phi(u,\mathbf{y})\delta(\boldsymbol{y}\cdot\bar{\boldsymbol{\beta}}-s)d\boldsymbol{y}, \qquad (\bar{\boldsymbol{\beta}},s)\in S^{n-2}\times\mathbb{R}.$$

Again, we notice that $R[\Phi(u,\cdot)](\bar{\boldsymbol{\beta}},s)$ is equal to zero for $|s|\ge 1$ since $\Phi(u,\boldsymbol{y})$ is supported in $|\boldsymbol{y}|<1$.

It is well known (see, e.g., [14, 15, 18, 22, 23]) that when $R\Phi$ is the m-dimensional regular Radon transform, we have for $\mathbf{y}=(y_1,y_2,\dots,y_m)\in\mathbb{R}^m$,

$$\Phi(u,\mathbf{y}) = \frac{(2\pi)^{1-m}}{2} \begin{cases} (-1)^{\frac{m-2}{2}} \displaystyle\int_{S^{m-1}} H_s \partial_s^{m-1} R\Phi(\boldsymbol{\beta},\boldsymbol{\beta}\cdot\mathbf{y}) dS(\boldsymbol{\beta}) & \text{if } m \text{ is even}, \\ (-1)^{\frac{m-1}{2}} \displaystyle\int_{S^{m-1}} \partial_s^{m-1} R\Phi(\boldsymbol{\beta},\boldsymbol{\beta}\cdot\mathbf{y}) dS(\boldsymbol{\beta}) & \text{if } m \text{ is odd}. \end{cases} \tag{3.7}$$

(Here we can use the inversion formula derived in [4] instead of (3.7) because $R\Phi$ is equal to zero for $|s|>1$.) Hence for $n\ge 3$, we have for $(u,\boldsymbol{\alpha})\in\mathbb{R}\times S^{n-1}$ and $\alpha_2\ge 0$,

(3.8)

$$\begin{aligned} &P_k f(u,\boldsymbol{\alpha}) \\ &= \frac{\alpha_2}{2}(2\pi)^{2-n} \begin{cases} (-1)^{\frac{n-3}{2}} \displaystyle\int_{S^{n-2}} H_s \partial_s^{n-2} C^k f(u,\bar{\boldsymbol{\beta}},\bar{\boldsymbol{\beta}}\cdot(\alpha_1,\alpha_3,\dots,\alpha_n)) dS(\bar{\boldsymbol{\beta}}) & \text{if } n \text{ odd}, \\ (-1)^{\frac{n-2}{2}} \displaystyle\int_{S^{n-2}} \partial_s^{n-2} C^k f(u,\bar{\boldsymbol{\beta}},\bar{\boldsymbol{\beta}}\cdot(\alpha_1,\alpha_3,\dots,\alpha_n)) dS(\bar{\boldsymbol{\beta}}) & \text{if } n \text{ even}. \end{cases} \end{aligned}$$

Since $P_k f(u,\mathbf{w}) = |\mathbf{w}|^{-k-1} P_k f(u,\mathbf{w}/|\mathbf{w}|)$, we have $P_k f(u,\mathbf{w})$ for $(u,\mathbf{w})\in\mathbb{R}\times\mathbb{R}^n$ from

$P_k f(u,\boldsymbol{\alpha})$ for $(u,\boldsymbol{\alpha}) \in \mathbb{R}\times S^{n-1}$: (3.8) becomes

(3.9)
$$P_k f(u,\mathbf{w}) = \frac{w_2(2\pi)^{2-n}}{2|\mathbf{w}|^{k+2}} \begin{cases} (-1)^{\frac{n-3}{2}} \displaystyle\int_{S^{n-2}} H_s \partial_s^{n-2} C^k f\left(u, \bar{\boldsymbol{\beta}}, \bar{\boldsymbol{\beta}}\cdot\frac{(w_1,w_3,\ldots,w_n)}{|\mathbf{w}|}\right) dS(\bar{\boldsymbol{\beta}}) \\ \quad \text{if } n \text{ odd}, \\ (-1)^{\frac{n-2}{2}} \displaystyle\int_{S^{n-2}} \partial_s^{n-2} C^k f\left(u, \bar{\boldsymbol{\beta}}, \bar{\boldsymbol{\beta}}\cdot\frac{(w_1,w_3,\ldots,w_n)}{|\mathbf{w}|}\right) dS(\bar{\boldsymbol{\beta}}) \\ \quad \text{if } n \text{ even}. \end{cases}$$

Combining Lemma 2 and (3.9), $I^{\kappa}_{x_1} f(\mathbf{x})$ is equal to

$$\frac{x_2}{2(2\pi)^{n-1}} \begin{cases} (-1)^{\frac{n-3}{2}} \displaystyle\int_{\mathbb{R}}\int_{S^{n-2}} I_u^{\kappa-1} H_s \partial_s^{n-2} C^k f\left(x_1 - w_1, \bar{\boldsymbol{\beta}}, \bar{\boldsymbol{\beta}}\cdot\frac{(w_1,x_3\ldots,x_n)}{|(w_1,\boldsymbol{x})|}\right) \frac{dS(\bar{\boldsymbol{\beta}})dw_1}{|(w_1,\boldsymbol{x})|^{k+2}} \\ \quad \text{if } n \text{ odd}, \\ (-1)^{\frac{n-2}{2}} \displaystyle\int_{\mathbb{R}}\int_{S^{n-2}} I_u^{\kappa-1} \partial_s^{n-2} C^k f\left(x_1 - w_1, \bar{\boldsymbol{\beta}}, \bar{\boldsymbol{\beta}}\cdot\frac{(w_1,x_3\ldots,x_n)}{|(w_1,\boldsymbol{x})|}\right) \frac{dS(\bar{\boldsymbol{\beta}})dw_1}{|(w_1,\boldsymbol{x})|^{k+2}} \\ \quad \text{if } n \text{ even}, \end{cases}$$

for $x_2 \geq 0$. ∎

Remark 6. Putting $n=3$, $k=1$, and $\kappa=0$ in (3.5) yields

$$\begin{aligned} f(x,y,z) &= \frac{y}{8\pi^2} C^{1,*}\left[H_u\partial_u H_s \partial_s C^1 f\left(u,\bar{\boldsymbol{\beta}},s\right)|(x,y,z)-(u,0,0)|^{-2}\right](x,y,z) \\ &= \frac{y}{8\pi^2}\int_{\mathbb{R}}\int_{S^1} H_u\partial_u H_s\partial_s C^1 f\left(x-w_1,\bar{\boldsymbol{\beta}},\frac{\bar{\boldsymbol{\beta}}\cdot(w_1,z)}{|(w_1,y,z)|}\right)\frac{dS(\bar{\boldsymbol{\beta}})dw_1}{|(w_1,y,z)|^3}. \end{aligned} \tag{3.10}$$

This inversion formula is implemented in section 4.

4. Numerical simulations.

In this section we numerically implement and verify the inversion formula given in Theorem 5, more precisely, formula (3.10). Indeed, we successfully demonstrate that the inversion formula recovers the original data f.

We test with $f = f(x,y,z)$,

$$\begin{aligned} &\text{(a)} \quad f = \chi_{0,2,0,0.4}\,(x,y,z), \\ &\text{(b)} \quad f = \chi_{0,1,1,0.5}\,(x,y,z) + \chi_{0,2.5,1,0.5}\,(x,y,z) + \chi_{0,1,2.5,0.5}\,(x,y,z), \end{aligned} \tag{4.1}$$

where $\chi_{a,b,c,R}(x,y,z) = 1$ if $(x,y,z)\in\mathcal{B}$ and 0 otherwise with

$$\mathcal{B} = \mathcal{B}(a,b,c,R) = \{(x,y,z)\in\mathbb{R}^3 : (x-a)^2+(y-b)^2+(z-c)^2 \leq R^2\}.$$

We then explicitly deduce the cone transform $Cf(u,\bar{\boldsymbol{\beta}},s) = C^1 f(u,\bar{\boldsymbol{\beta}},s)$ given in (2.4) for $f = \chi_{a,b,c,R}(x,y,z)$ with $\bar{\boldsymbol{\beta}} = (\cos\beta,\sin\beta)$. To obtain the cone transform, as noted in Theorem 5 we set f to be compactly supported in $y>0$. We notice that

$$\begin{aligned} Cf(u,\bar{\boldsymbol{\beta}},s) &= \int_{S^2}\int_0^{\infty} f((u,0,0)+r\boldsymbol{\alpha}) r\delta(\boldsymbol{\alpha}\cdot\boldsymbol{\beta}-s)drdS(\boldsymbol{\alpha}) \\ &= \int_0^{2\pi}\int_0^{\infty} f((u,0,0)+r\boldsymbol{\alpha}(\phi))rdrd\phi, \quad \boldsymbol{\alpha}\cdot\boldsymbol{\beta}=s, \boldsymbol{\alpha}\in S^2, \end{aligned} \tag{4.2}$$

as shown in (2.2). We then write

$$\boldsymbol{\beta} = (\cos\beta, 0, \sin\beta), \quad \boldsymbol{\beta}^{\perp} = (\cos\phi\sin\beta, -\sin\phi, -\cos\phi\cos\beta),$$

where ϕ is measured counterclockwise about the central axis $\boldsymbol{\beta}$ (see Figure 3). Observing that $\boldsymbol{\alpha}\cdot\boldsymbol{\beta} = s$ and $\boldsymbol{\alpha}\cdot\boldsymbol{\beta}^{\perp} = \sqrt{1-s^2}$ we can explicitly express $\boldsymbol{\alpha}$,

$$\begin{aligned}\boldsymbol{\alpha} &= (\boldsymbol{\alpha}\cdot\boldsymbol{\beta})\boldsymbol{\beta} + (\boldsymbol{\alpha}\cdot\boldsymbol{\beta}^{\perp})\boldsymbol{\beta}^{\perp} \\ &= \left(s\cos\beta + \sqrt{1-s^2}\cos\phi\sin\beta, -\sqrt{1-s^2}\sin\phi, s\sin\beta - \sqrt{1-s^2}\cos\phi\cos\beta\right).\end{aligned} \tag{4.3}$$

Note that r is the distance from $(u,0,0)$ and the line $(u,0,0)+r\boldsymbol{\alpha}$ meets the sphere $(\partial\mathcal{B})$ twice at $r = r_1$ and r_2 $(r_1 > r_2 \geq 0)$. Then the inner integral of (4.2) is reduced to $\int_0^{\infty}\chi_{a,b,c,R}((u,0,0)+r\boldsymbol{\alpha}(\phi))rdr = \int_{r_1}^{r_2} rdr$. We need to find $r = r_1, r_2$ $(r_1 > r_2 \geq 0)$ at which the line intersects the sphere. Writing $\mathbf{a} = (a,b,c)$ we solve for r:

$$R^2 = |(u,0,0) + r\boldsymbol{\alpha} - \mathbf{a}|^2 = r^2 + 2r\boldsymbol{\alpha}\cdot((u,0,0)-\mathbf{a}) + |(u,0,0)-\mathbf{a}|^2.$$

That is, we solve

$$r^2 - 2g(\phi)r + (u-a)^2 + b^2 + c^2 - R^2 = 0,$$

where, thanks to (4.3),

$$\begin{aligned}g(\phi) = -\boldsymbol{\alpha}\cdot((u,0,0)-\mathbf{a}) &= -s((u-a)\cos\beta - c\sin\beta) \\ &\quad - \sqrt{1-s^2}((u-a)\cos\phi\sin\beta + b\sin\phi + c\cos\phi\cos\beta).\end{aligned}$$

Then the solutions are $r_1 = g^+(\phi) + \sqrt{D^+}$ and $r_2 = g^+(\phi) - \sqrt{D^+}$, where

$$D = \Big(g(\phi)\Big)^2 - \Big((u-a)^2 + b^2 + c^2 - R^2\Big), \quad D^+ = \max\{D,0\},\ g^+ = \max\{g,0\}.$$

Here, since $\partial\mathcal{B} \subset \{(x,y,z)\in\mathbb{R}^3 : y > 0\}$, we note that the line $(u,0,0)+r\boldsymbol{\alpha}$, $r \geq 0$, meets $\partial\mathcal{B}$ if and only if $D \geq 0$ and $g(\phi) \geq 0$.

From (4.2) the cone transform is thus explicitly found as follows:

$$\begin{aligned}Cf(u,\bar{\boldsymbol{\beta}},s) &= \int_{S^2}\int_0^{\infty}\chi_{a,b,c,R}((u,0,0)+r\boldsymbol{\alpha})\delta(\boldsymbol{\alpha}\cdot\boldsymbol{\beta}-s)rdrdS(\boldsymbol{\alpha}) = \int_0^{2\pi}\int_{r_2}^{r_1} rdrd\phi \\ &= \frac{1}{2}\int_0^{2\pi}(r_1+r_2)(r_1-r_2)d\phi = 2\int_0^{2\pi} g^+(\phi)\sqrt{D^+}d\phi.\end{aligned} \tag{4.4}$$

For f in (a) of (4.1), the corresponding cone transform $Cf(u,\bar{\boldsymbol{\beta}},s)$ is plotted in Figure 4. Thanks to the linearity underlying the cone transform and its inverse, superposing the cone transforms we can also explicitly find the cone transform for f in (b) of (4.1).

Once we obtain the cone transform data $Cf = C^1 f$ given in (4.4) for $k = 1$, we now numerically test the inversion formula. Equivalently, we write it as follows. Assuming that

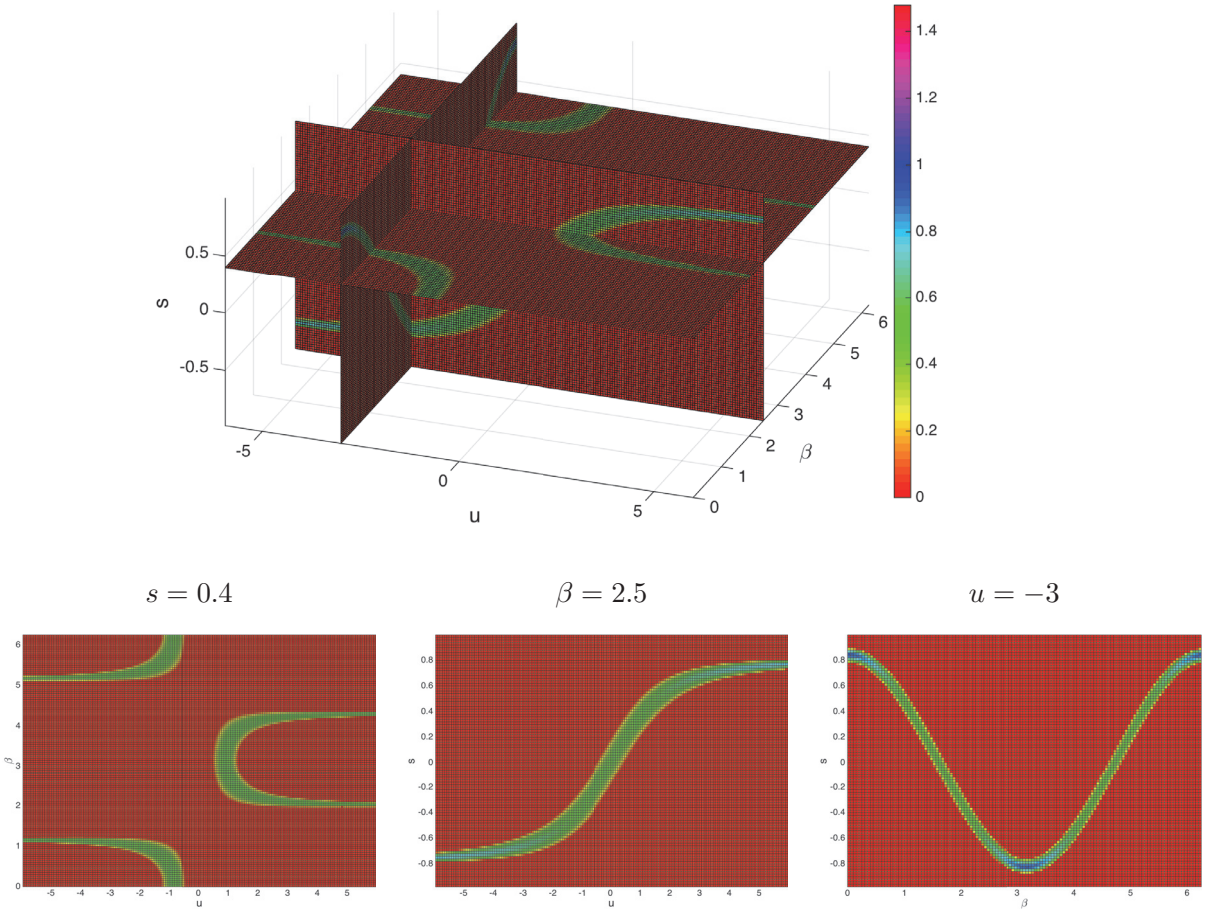

Figure 4. *Slices for $Cf(u, \bar{\boldsymbol{\beta}}, s)$ corresponding to $f = \chi_{0,2,0,0.4}(x, y, z)$ in (a); $u \in [-6, 6]$, $\beta \in [0, 2\pi)$, and $s \in [-1, 1]$.*

$f(x, y, z)$ is compactly supported in $y > 0$, since the Fourier transform of $H_u(\partial_u h)(t)$ is $-i \cdot sgn(\xi)\mathcal{F}_{u\to\xi}(\partial_u h)(\xi) = |\xi|\mathcal{F}_{u\to\xi}h(\xi)$, we can rewrite the inversion formula (3.10):

(4.5)

$$f(x,y,z) = \frac{y}{8\pi^2}\int_{\mathbb{R}}\int_0^{2\pi} \mathcal{F}^{-1}_{(\xi,\sigma)\to(u,s)}\left[|\xi||\sigma|\mathcal{F}_{(u,s)\to(\xi,\sigma)}Cf(u,\cdot,s)\right]\left(x - w_1, \bar{\boldsymbol{\beta}}, \frac{\bar{\boldsymbol{\beta}}\cdot(w_1,z)}{|(w_1,y,z)|}\right)\frac{d\beta dw_1}{|(w_1,y,z)|^3},$$

where $\bar{\boldsymbol{\beta}} = (\cos\beta, \sin\beta)$ and $\mathcal{F}_{(u,s)\to(\xi,\sigma)}h(\xi,\sigma)$ is the 2-dimensional Fourier transform of $h(u,s)$ with respect to u and s and $\mathcal{F}^{-1}_{(\xi,\sigma)\to(u,s)}$ is its inverse Fourier transform.

The inversion formula (4.5) is easily evaluated on parallel machines by decomposing the computational domain $\{(x, y, z)\}$ because the evaluation on each point is completely independent. This can substantially save time. However, we note that the integrand in (4.5) involves the singular terms which diverge to ∞ as $(y, z) \to (0, 0)$. The singular terms have to be treated with special care in the numerical integrations where the accuracy depends on the location of the point (x, y, z). For example, since w_1 attains zero, if y and z are close to zero, we expect

that the numerical evaluation for the formula blows up. To avoid it, we position the compact support of f away from the plane $y = 0$ which is assumed to be in $y > 0$.

We also note that in the cone transform and its inversion, (4.4) and (4.5), whereas the parameters β and s are in bounded intervals, i.e., $[0, 2\pi]$ and $[-1, 1]$, respectively, the ranges of u, w_1 in Cf and its inversion are $(-\infty, \infty)$. This makes the computations subtle. Although it turns out that the inversion formula is not difficult to implement, due to the computational restrictions for the ranges of u in Cf and of w_1 in its inversion (4.5), we note that in the parts near the north and south poles there are some defects (inaccuracies) of the inversion which can be explained as follows.

As noted in Figure 4, the cone transform data Cf is 2π-periodic in β, supported in $s \in [-1, 1]$ but the data are truncated at $u = \pm L$, i.e., we need to restrict u on $[-L, L]$ for computations. Throughout the simulations, we use $L = 6$. Hence, due to the limitation of u, some parts of f are not properly transformed via the cone transform (4.2) in the regions near the north and south poles, and those parts cannot be properly reconstructed as noted in Figure 5. Furthermore, the inversion formula (4.5) also has a computational limitation in the interval of integration for w_1. We have to truncate the range of w_1 at, e.g., $w_1 = \pm W$ (we use $W = 8$ in the simulations). In addition, due to the periodic nature of the built-in fast Fourier transform (FFT) (e.g., *fft2*, *ifft2*) in MATLAB, the FFTs for $\mathcal{F}$ and $\mathcal{F}^{-1}$ have limitations in dealing with the nonperiodicity of Cf in u.

To verify stability numerically in the inversion formula, we also test with the cone transform data $\tilde{C}f$ involving an additive white Gaussian noise (WGN) with intensities $p = 0.2$ and 2,

$$\tilde{C}f(u, \bar{\boldsymbol{\beta}}, s) = Cf(u, \bar{\boldsymbol{\beta}}, s) + p \times WGN. \tag{4.6}$$

Here WGN is a white Gaussian noise with mean 0 and variance 1. Figure 6 shows that the balls are well reconstructed. Indeed, the reconstruction is robust with respect to noise.

Finally, we take a 3-dimensional phantom which consists of the four balls, $\mathcal{B}(0, 2, 0, 0.4)$, $\mathcal{B}(0, 2.5, 0, 0.5)$, $\mathcal{B}(-0.3, 2, 0, 0.8)$, and $\mathcal{B}(-1, 1, 0.05, 0.2)$ (see Figure 7). This figure shows the slices $z = 0$ for the original phantom and the reconstructed image via (4.5). The cone transform Cf is obtained by transforming the four balls via (4.4). Here, to show more clear and accurate images, we use the truncations $L = 16$ and $W = 18$. Indeed, compared with the results which use $L = 6$ and $W = 8$, the accuracy is much better and the balls are clearly identified. This implies that the truncations in the implementations are crucial. The reasons are as follows. The inversion formula (4.5) involves the so-called filter followed by the backprojection. The filter is composed of four operations, i.e., two differentiations and two Hilbert transforms,

$$H_u H_s \Big[\partial_u \partial_s Cf\Big] = \mathcal{F}^{-1}_{(\xi,\sigma)\to(u,s)} \Big[|\xi||\sigma| \mathcal{F}_{(u,s)\to(\xi,\sigma)} Cf\Big].$$

The Hilbert transforms or the Fourier transforms are nonlocal and need all information over the whole space $\mathbb{R}$ (see (3.3) above). The truncations in numerical implementations will then lead to the loss of information. In summary, the inversion formula (4.5) goes through two multiplications by the magnitude of the frequency and three truncations for the Fourier and inverse Fourier transforms, and backprojection, respectively. As one can see from (4.4) and

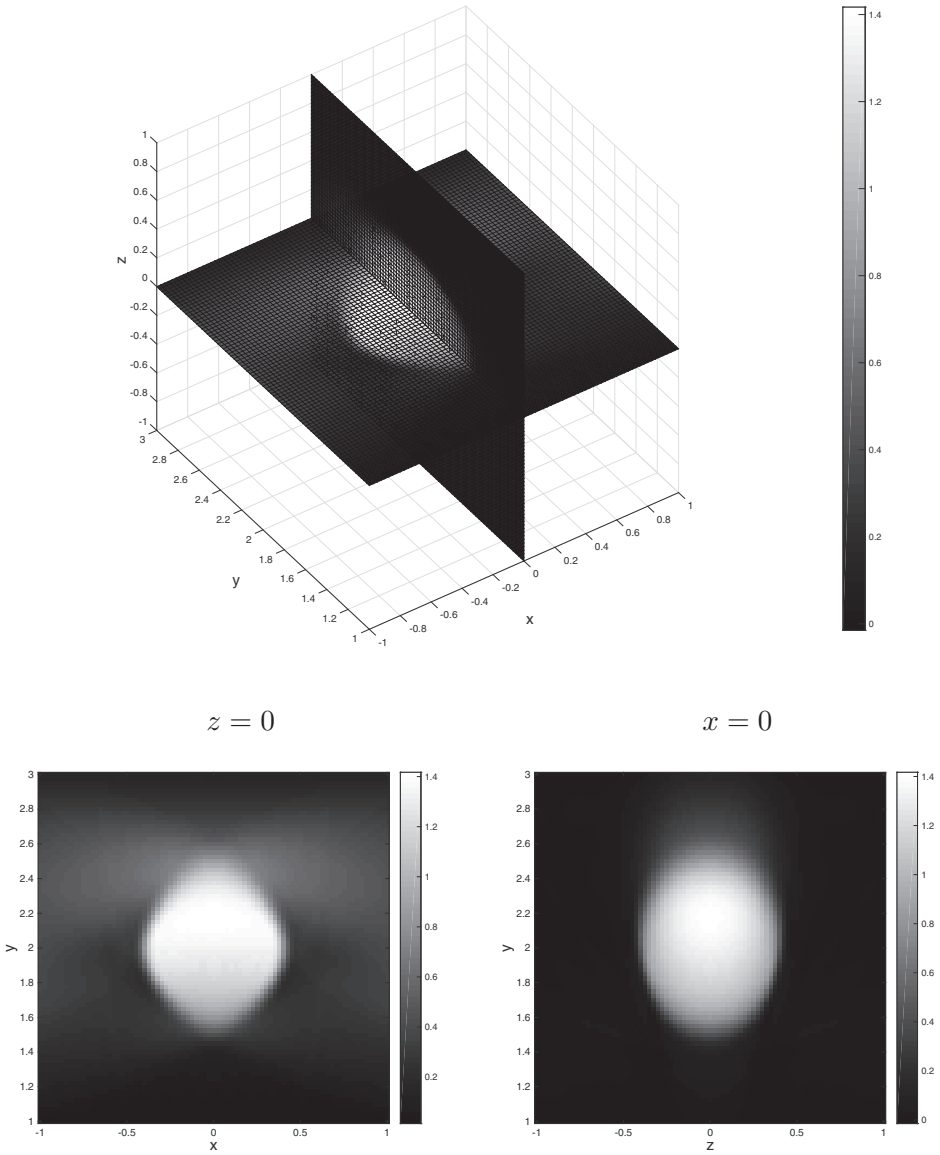

Figure 5. *Reconstruction from the cone transform data for* $f = \chi_{0,2,0,0.4}(x, y, z)$ *as in* (a) *of* (4.1).

Figure 4, the cone data Cf show singularities of a square-root-type which correspond to high frequencies in the Fourier transforms. Then the magnitudes of frequencies $|\xi|$ and $|\sigma|$ are multiplied which make the high frequency data very weighted. Truncations of these high frequency data give considerable loss of information which yields poor quality of the image reconstructions.

Other than resolving the truncation issues, to obtain clear images, we can try to strengthen the filtration (see, e.g., [18]). For example, we can replace the filtration $H_s\partial_s$ with the second derivative which preserves the singularities well, i.e., edges or boundaries (see, e.g., [8, 17]). However, the numerical issues such as the filtration techniques, deblurring, and improving

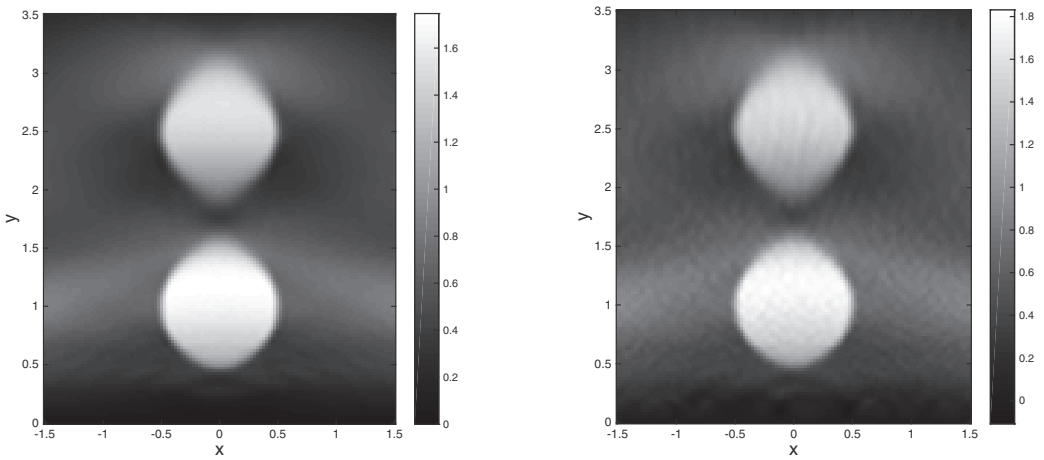

Figure 6. *Slice $z = 1$ corresponding to f as in* (b) *of* (4.1); *(left) Reconstruction from* (4.6) *with noise $p = 0.2$; (right) with $p = 2$.*

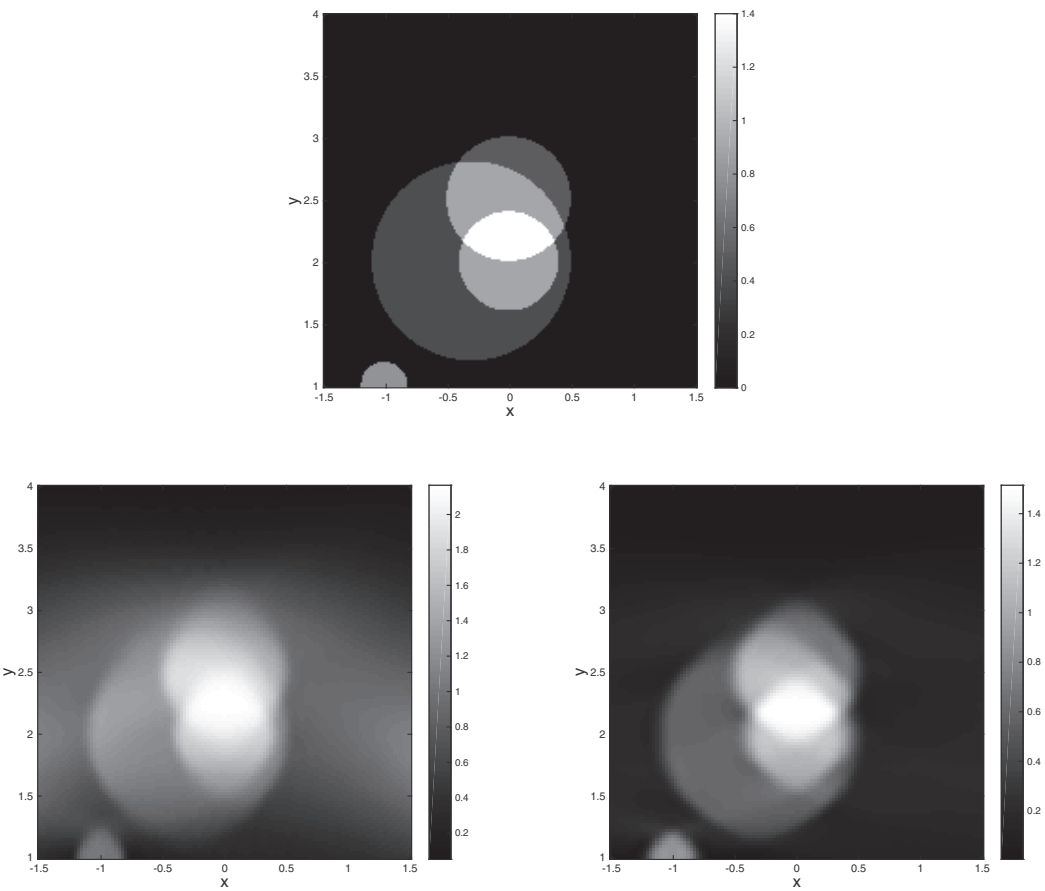

Figure 7. *Slice $z = 0$: (top) 3-dimensional phantom; Numerical inversion via* (4.5) *with (left) $L = 6, W = 8$ and (right) $L = 16, W = 18$.*

numerical errors are considerable subjects and they will be discussed and developed in forthcoming works.

REFERENCES

[1] M. Allmaras, D.P. Darrow, Y. Hristova, G. Kanschat, and P. Kuchment, *Detecting small low emission radiating sources*, Inverse Probl. Imaging, 7 (2013), pp. 47–79.

[2] R. Basko, G.L. Zeng, and G.T. Gullberg, *Application of spherical harmonics to image reconstruction for the Compton camera*, Phys. Med. Biol., 43 (1998), pp. 887–894.

[3] J.W. LeBlanc, N.H. Clinthorne, C.-H. Hua, E. Nygard, W.L. Rogers, D.K. Wehe, P. Weilhammer, and S.J. Wilderman, *C-sprint: A prototype Compton camera system for low energy gamma ray imaging*, IEEE Trans. Nucl. Sci., 45 (1998), pp. 943–949.

[4] A.M. Cormack, *Representation of a function by its line integrals, with some radiological applications*, J. Appl. Phys., 34 (1963), pp. 2722–2727.

[5] J. Cebeiro, M. Morvidone, and M.K. Nguyen, *Back-projection inversion of a conical radon transform*, Inverse Probl. Sci. Eng., 24 (2016), pp. 328–352.

[6] M.J. Cree and P.J. Bones, *Towards direct reconstruction from a gamma camera base on Compton scattering*, IEEE Trans. Med. Imaging, 13 (1994), pp. 398–409.

[7] D.B. Everett, J.S. Fleming, R.W. Todd, and J.M. Nightingale, *Gamma-radiation imaging system based on the Compton effect*, Proceedings of the Institution of Electrical Engineers, 124 (1977), pp. 995–1000.

[8] A. Faridani, E.L. Ritman, and K.T. Smith, *Local tomography*, SIAM J. Appl. Math., 52 (1992), pp. 459–484.

[9] D. V. Finch and D. C. Solmon, *A characterization of the range of the divergent beam X-ray transform*, SIAM J. Math. Anal., 14 (1983), pp. 767–771.

[10] D.V. Finch, *Cone beam reconstruction with sources on a curve*, SIAM J. Appl. Math., 45 (1985), pp. 665–673.

[11] R. Gouia-Zarrad, *Analytical reconstruction formula for n-dimensional conical Radon transform*, Comput. Math. Appl., 68 (2014), pp. 1016–1023.

[12] R. Gouia-Zarrad and G. Ambartsoumian, *Exact inversion of the conical Radon transform with a fixed opening angle*, Inverse Problems, 30 (2014), 045007.

[13] M. Haltmeier, *Exact reconstruction formulas for a Radon transform over cones*, Inverse Problems, 30 (2014), 035001.

[14] S. Helgason, *The Radon Transform*, Progr. Math. 5, Birkhäuser, Boston, 1999.

[15] S. Helgason, *Integral Geometry and Radon Transforms*, Springer, New York, 2011.

[16] C. Jung and S. Moon, *Inversion formulas for cone transforms arising in application of Compton cameras*, Inverse Problems, 31 (2015), 015006.

[17] P. Kuchment, K. Lancaster, and L. Mogilevskaya, *On local tomography*, Inverse Problems, 11 (1995), pp. 571–590.

[18] P. Kuchment, *The Radon Transform and Medical Imaging*, CBMS-NSF Regional Conf. Ser. Appl. Math. 85, SIAM, Philadelphia, 2014.

[19] V. Maxim, M. Frandeş, and R. Prost, *Analytical inversion of the Compton transform using the full set of available projections*, Inverse Problems, 25 (2009), 095001.

[20] S. Moon, *Inversions of the windowed ray transform*, J. Inverse Ill-Posed Probl., to appear.

[21] S. Moon, *On the determination of a function from its conical Radon transform with fixed central axis*, SIAM J. Math. Anal., to appear.

[22] F. Natterer, *The Mathematics of Computerized Tomography*, Classics Appl. Math. 32, SIAM, Philadelphia, 2001.

[23] F. Natterer and F. Wübbeling, *Mathematical Methods in Image Reconstruction*, SIAM Monogr. Math. Model. Comput., SIAM, Philadelphia, 2001.

[24] M.K Nguyen, T.T Truong, H.D Bui, and J.L Delarbre, *A novel inverse problem in γ-rays emission imaging*, Inverse Probl. Sci. Eng., 12 (2004), pp. 225–246.

[25] M.K. Nguyen, T.T. Truong, and P. Grangeat, *Radon transforms on a class of cones with fixed axis direction*, J. Phys. A, 38 (2005), pp. 8003–8015.
[26] M. Singh, *An electronically collimated gamma camera for single photon emission computed tomography. Part* I: *Theoretical considerations and design criteria*, Med. Phys., 10 (1983), pp. 421–427.
[27] B. Smith, *Cone-beam tomography: Recent advances and a tutorial review*, Opt. Eng., 29 (1990), pp. 524–534.
[28] B. Smith, *Reconstruction methods and completeness conditions for two Compton data models*, J. Opt. Soc. Amer. A, 22 (2005), pp. 445–459.
[29] K.T. Smith, D.C. Solmon, and S.L. Wagner, *Practical and mathematical aspects of the problem of reconstructing a function from radiographs*, Bull. Amer. Math. Soc., 82 (1977), pp. 1227–1270.
[30] D.C. Solmon, *X-ray transform*, J. Math. Anal. Appl., 56 (1976), pp. 61–83.
[31] F. Terzioglu, *Some inversion formulas for the cone transform*, Inverse Problems, 31 (2015), 115010.
[32] R.W. Todd, J.M. Nightingale, and D.B. Everett, *A proposed gamma camera*, Nature, 251 (1974), pp. 132–134.
[33] H.K. Tuy, *An inversion formula for cone-beam reconstruction*, SIAM J. Appl. Math., 43 (1983), pp. 546–552.
[34] T.T. Truong, M.K. Nguyen, and H. Zaidi, *The mathematical foundations of* 3*D Compton scatter emission imaging*, Internat. J. Biomed. Imaging, (2007), 92780.